

Cite this: *Dalton Trans.*, 2021, **50**, 14432

## Electronic structures and spectroscopic signatures of diiron intermediates generated by O<sub>2</sub> activation of nonheme iron(II)-thiolate complexes†

Danushka M. Ekanayake,<sup>a</sup> Dao Pham,<sup>b</sup> Andrew L. Probst,<sup>b</sup> Joshua R. Miller,<sup>c</sup> Codrina V. Popescu <sup>b</sup> and Adam T. Fiedler <sup>a\*</sup>

The activation of O<sub>2</sub> at thiolate-ligated iron(II) sites is essential to the function of numerous metalloenzymes and synthetic catalysts. Iron-thiolate bonds in the active sites of nonheme iron enzymes arise from either coordination of an endogenous cysteinate residue or binding of a deprotonated thiol-containing substrate. Examples of the latter include sulfoxide synthases, such as EgtB and OvoA, that utilize O<sub>2</sub> to catalyze tandem S-C bond formation and S-oxygenation steps in thiohistidine biosyntheses. We recently reported the preparation of two mononuclear nonheme iron-thiolate complexes (**1** and **2**) that serve as structural active-site models of substrate-bound EgtB and OvoA (*Dalton Trans.* 2020, **49**, 17745–17757). These models feature monodentate thiolate ligands and tripodal N<sub>4</sub> ligands with mixed pyridyl/imidazolyl donors. Here, we describe the reactivity of **1** and **2** with O<sub>2</sub> at low temperatures to give metastable intermediates (**3** and **4**, respectively). Characterization with multiple spectroscopic techniques (UV-vis absorption, NMR, variable-field and -temperature Mössbauer, and resonance Raman) revealed that these intermediates are thiolate-ligated iron(III) dimers with a bridging oxo ligand derived from the four-electron reduction of O<sub>2</sub>. Structural models of **3** and **4** consistent with the experimental data were generated via density functional theory (DFT) calculations. The combined experimental and computational results illuminate the geometric and electronic origins of the unique spectral features of diiron(III)-μ-oxo complexes with thiolate ligands, and the spectroscopic signatures of **3** and **4** are compared to those of closely-related diiron(III)-μ-peroxo species. Collectively, these results will assist in the identification of intermediates that appear on the O<sub>2</sub> reaction landscapes of iron-thiolate species in both biological and synthetic environments.

Received 10th July 2021,  
Accepted 12th September 2021  
DOI: 10.1039/d1dt02286e  
[rsc.li/dalton](http://rsc.li/dalton)

### I. Introduction

In addition to their ubiquitous presence in iron-sulfur clusters, iron-thiolate bonds are found in several metalloenzymes that activate O<sub>2</sub> or its reduced derivatives (O<sub>2</sub><sup>-</sup>, H<sub>2</sub>O<sub>2</sub>). In cytochrome P450s, the iron-thiolate unit arises from coordination of an axial cysteinate (Cys), which has been shown to enhance the potency of the active compound I intermediate.<sup>1–4</sup> Similarly, the thiolate ligand of superoxide reductase (SOR) plays a critical role in modulating the redox potential, spin

state, and lability of the nonheme iron center.<sup>5–8</sup> In other enzymes, the iron-thiolate bond arises when a sulfur-containing substrate binds to a mononuclear nonheme iron center within the active site. Examples include isopenicillin N synthase (IPNS),<sup>9</sup> cysteine dioxygenase (CDO),<sup>10–12</sup> sulfoxide synthases,<sup>13,14</sup> and persulfide dioxygenase.<sup>15,16</sup> These enzymes follow a mechanism in which thiolate coordination is followed by O<sub>2</sub> binding, giving rise to an iron(III)-superoxide intermediate.<sup>17,18</sup> The highly covalent nature of the Fe-S bond facilitates subsequent formation of iron-peroxo and -oxo intermediates in the catalytic cycle.<sup>19,20</sup> These short-lived species have largely eluded spectroscopic detection to date, although some attempts to trap and characterize IPNS and CDO intermediates using transient absorption and freeze-quench methods have been successful.<sup>21,22</sup>

In recent years, there have been numerous reports of synthetic complexes that mimic the active-site structures of thiol-oxidizing nonheme iron enzymes.<sup>23,24</sup> Small-molecule models of thiol dioxygenases, such as CDO and cysteamine dioxygen-

<sup>a</sup>Department of Chemistry, Marquette University, Milwaukee, Wisconsin 53233, USA.  
E-mail: adam.fiedler@marquette.edu; Fax: (+1) 414-288-7066

<sup>b</sup>Department of Chemistry, The College of Arts and Sciences, University of St. Thomas, St. Paul, Minnesota 55105, USA. E-mail: ewba2202@stthomas.edu

<sup>c</sup>Department of Chemistry, University of Wisconsin – Madison, Madison, Wisconsin 53706, USA

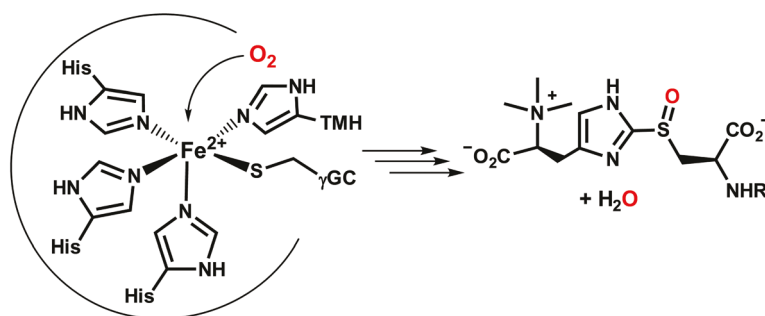
† Electronic supplementary information (ESI) available. See DOI: 10.1039/d1dt02286e

ase, have been shown to replicate the enzymatic reactivity by generating *S*-dioxygenated products upon exposure to  $O_2$ .<sup>25–29</sup> In some cases, CDO models react with  $O_2$  to yield metastable iron(III)-superoxo<sup>30,31</sup> and iron(IV)-oxo<sup>32</sup> species that have been investigated with spectroscopic methods, thereby providing valuable precedents for putative enzymatic intermediates. The Kovacs group has also generated iron(III)-hydroperoxo species by treating iron(II)-thiolate complexes with  $KO_2$  in the presence of  $H^+$  donors.<sup>33,34</sup> Because the iron centers of the synthetic models are not buried within enzyme active sites, reactions with  $O_2$  often result in thiolate-ligated iron(III) dimers featuring  $\mu$ -(hydr)oxo or  $\mu$ -peroxo bridges.<sup>32,35–40</sup> Similar intermediates have been observed for diiron(II)-thiolate complexes that behave as  $O_2$  reduction catalysts in the presence of electron and proton donors.<sup>41–43</sup>

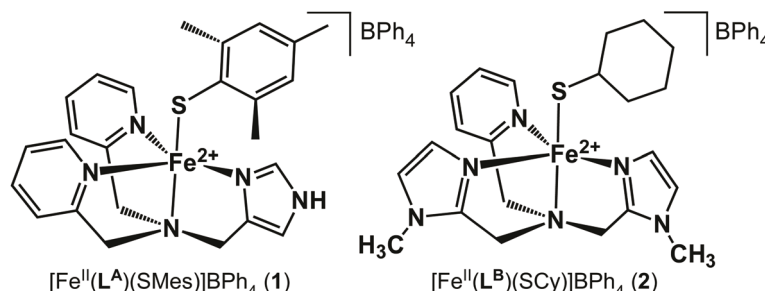
Recently, we reported the synthesis of two nonheme iron(II)-thiolate complexes that serve as active-site models of EgtB and OvoA – the two known sulfoxide synthases.<sup>44</sup> These mononuclear nonheme iron enzymes catalyze the  $O_2$ -dependent formation of a S–C bond between His- and Cys-derived molecules, in conjunction with S-atom monooxygenation.<sup>20,45,46</sup> X-ray crystal structures of EgtB revealed that the monoiron(II) center is bound to three His residues in a facial orientation; the  $\gamma$ -glutamyl-L-cysteine and *N*- $\alpha$ -trimethyl histidine substrates coordinate at adjacent sites *via* their imidazole and thiolate groups, respectively (Scheme 1).<sup>13,14,47,48</sup> Our synthetic EgtB and OvoA models, shown in Scheme 2, are based on tetradentate  $N_4$  chelates ( $L^A$  and  $L^B$ ) that consist of one or two pendant imidazole donors.

Attachment of a monodentate aryl or alkyl thiolate ligand yields the five-coordinate Fe(II) complexes  $[Fe^{II}(L^A)(SMes)]BPh_4$  (**1**) and  $[Fe^{II}(L^B)(SCy)]BPh_4$  (**2**), where SMes = 2,4,6-trimethylthiophenolate and SCy = cyclohexanethiolate. The *cis*-arrangement of thiolate and imidazole donors in the X-ray structures of **1** and **2** resembles the geometry of substrate-bound SO synthases. Both complexes react with nitric oxide (NO) to generate six-coordinate  $\{FeNO\}^+$  adducts.

Exposure of **1** and **2** to  $O_2$  does not lead to products arising from C–S bond formation or *S*-oxygenation; instead, the thiolate ligands undergo oxidative S–S bond formation to generate disulfide byproducts.<sup>44</sup> However, it was noted that reaction of **2** with  $O_2$  at room temperature generates a short-lived purple intermediate. A similar species was subsequently observed at lower temperatures in aerobic solutions of complex **1**. The nature of these intermediates is the focus of the present work. Because the reaction of iron-thiolate complexes with  $O_2$  can yield a variety of monoiron and diiron species (*vide supra*), it was necessary to employ multiple spectroscopic techniques (UV-vis absorption, resonance Raman, and Mössbauer) to elucidate the identities of these  $O_2$ -derived species. Our experimental data indicate that the observed intermediates feature a diiron(III)- $\mu$ -oxo core and two terminal thiolate ligands. The electronic-structure origins of these spectral features are further probed through density functional theory (DFT) calculations. In the Discussion section, we compare the spectroscopic signatures of thiolate-ligated diiron(III)- $\mu$ -oxo complexes to those reported in the literature for closely-related species, in particular diiron(III)- $\mu$ -peroxo species.



Scheme 1 Substrate-bound active site and product of EgtB.



Scheme 2 Structures of complexes **1** and **2**.

## II. Experimental and computational methods

### Materials

The Fe(II) precursor complexes (**1** and **2**) were prepared using procedures described in our previous report.<sup>44</sup> Complexes were handled under an inert atmosphere using a Vacuum Atmospheres Omni-Lab glovebox. Dichloromethane and acetonitrile solvents were dried over  $\text{CaH}_2$  or  $\text{NaH}$ , followed by distillation and storage in the glovebox over activated molecular sieves. Deuterated solvents were purchased from Cambridge Isotope Laboratories, Inc. (Tewksbury, MA). Isotopically enriched  $\text{H}_2^{18}\text{O}_2$  (90%) was purchased from ICON/Berry & Associates (Dexter, MI) and  $^{18}\text{O}_2$  gas (99%) was purchased from Sigma-Aldrich. Scrambled  $\text{O}_2$  consisting of a statistical mixture of  $^{16}\text{O}_2$ ,  $^{16}\text{O}^{18}\text{O}$ , and  $^{18}\text{O}_2$  was prepared by following the procedure described by Proniewicz and Kincaid.<sup>49</sup> The presence and relative amounts of all three isotopomers was confirmed by GC-MS instrumentation (Agilent 5973 mass spectrometer attached to a 6850 gas chromatography system). While a statistical 1:2:1 ratio of  $^{16}\text{O}_2$ : $^{16}\text{O}^{18}\text{O}$ : $^{18}\text{O}_2$  is expected for scrambled  $\text{O}_2$ , the gas employed in these studies had the following composition:  $^{16}\text{O}_2$  (20%),  $^{16}\text{O}^{18}\text{O}$  (49%),  $^{18}\text{O}_2$  (31%). The discrepancy between the theoretical and actual isotopomeric ratios arose from a slight imbalance in the initial  $^{16}\text{O}_2$  and  $^{18}\text{O}_2$  levels prior to scrambling.

### Sample preparation

Intermediates **3** and **4** were generated by treating the precursor complexes (**1** and **2**, respectively) with various oxidants ( $\text{O}_2$ ,  $\text{H}_2\text{O}_2$ , or iodosylbenzene) at temperatures indicated in the text. Resonance Raman (rRaman) samples of **3** and **4** were prepared by adding solutions of the precursor complexes (concentrations between 10 and 12 mM) to NMR tubes under anaerobic conditions, followed by freezing in liquid nitrogen. Dioxygen-treated samples were attached to a Schlenk line and three vacuum/argon cycles were performed. The samples were then exposed to gaseous dioxygen ( $^{16}\text{O}_2$ ,  $^{18}\text{O}_2$ , or scrambled  $\text{O}_2$ ) and allowed to warm to either  $-78\text{ }^\circ\text{C}$  ( $\text{CD}_2\text{Cl}_2$ ) or  $-40\text{ }^\circ\text{C}$  ( $\text{CH}_3\text{CN}$ ). After the color change to green (**3**) or purple (**4**) was complete ( $\sim 1$  min), the samples were refrozen in liquid nitrogen and removed from the Schlenk line. For rRaman samples generated using  $\text{H}_2\text{O}_2$ , frozen solutions of the Fe(II) precursors were melted under anaerobic conditions at  $-40\text{ }^\circ\text{C}$ , followed by injection of an excess amount (5 eq.) of  $\text{H}_2\text{O}_2$  (or  $\text{H}_2^{18}\text{O}_2$ ) in  $\text{CH}_3\text{CN}$ . The solutions were mixed with a Vortex stirrer for a short time ( $\sim 5$  s.) and then refrozen. Mössbauer samples consisted of frozen butyronitrile solutions of **3** and **4** at high concentration ( $\sim 50$  mM). The Fe(II) precursor complexes were exposed to  $\text{O}_2$  at low temperature ( $-78\text{ }^\circ\text{C}$ ) and the resulting solutions were quickly transferred to pre-cooled Delrin cups (1.00 mL), then frozen in liquid nitrogen.

### Spectroscopic methods

Variable-temperature UV-vis absorption spectra were collected with an Agilent 8453 diode array spectrometer equipped with a

Unisoku Scientific Instruments cryostat (Osaka, Japan).  $^1\text{H}$  NMR spectra were measured on a Varian 400 MHz spectrometer. The resonance Raman data were measured using either 647.1 nm excitation from a Coherent I-302C  $\text{Kr}^+$  laser or 501.7 nm excitation from a Coherent I-305  $\text{Ar}^+$  laser. The frozen samples were held at 77 K in a liquid  $\text{N}_2$  dewar and the laser power at the sample ranged between 20 and 30 mW. The scattered light was collected using an Acton Research triple monochromator (1200 grooves per mm grating) paired with a Princeton Instruments Spec X:100BR deep depletion, back-thinned CCD camera. Baselines of the rRaman spectra were corrected using the software program SpectraGryph (<https://www.effemm2.de>). Digital addition of rRaman spectra were performed using the program IGOR. Peak energies were calibrated with reference to solvent peaks and the most intense peak of  $\text{K}_2\text{SO}_4$  ( $984\text{ cm}^{-1}$ ).

Mössbauer spectra were recorded on Janis cryostats running in constant accelerator mode. The low-field spectra were collected on a closed-cycle refrigerator spectrometer, model CCR4K (SeeCo, Edina, MN) equipped with a 0.07 T permanent magnet, maintaining temperatures between 6 and 300 K. High-field spectra were collected on a Super-Varitemp dewar equipped with a superconducting magnet allowing fields up to 7.0 T (Dr Yisong Guo, Carnegie Mellon University). The isomer shifts are quoted at 6 K with respect to an iron metal standard at 298 K. The Mössbauer spectra were analyzed using the software WMOSS4 (Ion Prisecaru, <https://www.wmoss.org>) and Spincount (Dr Michael Hendrich, Carnegie Mellon University). Spectral simulation and least-square fits were produced using the quadrupole interaction Hamiltonian (eqn (1)) appended with the spin Hamiltonian for the electronic spins (eqn (2)) of high-spin Fe(III) and Fe(II) centers. In addition, for the analysis of spin-coupled compounds, the exchange coupling term ( $\hat{H}_e = -2JS_1S_2$ ) was appended. In this convention, antiferromagnetic coupling corresponds to  $J < 0$  such that ground state is the one with the minimal spin ( $m_s = 0$  in this case).

$$\hat{H}_Q = \frac{eQV_{zz,i}}{12} \left[ \hat{I}_{z,i}^2 - \frac{15}{4} + \eta(\hat{I}_{x,i}^2 - \hat{I}_{y,i}^2) \right] \quad (1)$$

$$\begin{aligned} \hat{H}_S = & D \left[ S_z^2 - \frac{1}{3}S(S+1) + \frac{E}{D}(S_x^2 - S_y^2) \right] \\ & + \beta \hat{S} \cdot \vec{g} \cdot \vec{B} + \hat{S} \cdot \vec{A}_i \cdot \hat{I} + \hat{H}_Q(i) - g_n \beta_n \vec{B} \cdot \hat{I} \end{aligned} \quad (2)$$

### Computational methods

Density functional theory (DFT) calculations were performed within the ORCA 4.0 software package developed by Dr F. Neese.<sup>50,51</sup> Computational models of the diferric- $\mu$ -oxo intermediates (**3**<sup>DFT</sup> and **4**<sup>DFT</sup>), as well as the hypothetical  $\mu$ -1,2-peroxy species (**P1** and **P2**), were generated via unconstrained geometry optimizations. The **L<sup>B</sup>** ligand was modified by replacing the *N*-Me groups of the imidazole rings with H-atoms. In addition, the cyclohexyl ring of the SCy ligand was truncated to an isopropyl group and the methyl substituents of the SMes ligand were replaced with H-atoms. Optimized geometries

were calculated using the non-hybrid Becke-Perdew (BP86) functional<sup>52,53</sup> and numerical frequency calculations confirmed that all structures correspond to a local energy minima. Calculations utilized the Karlsruhe valence triple- $\zeta$  basis set combined with polarization functions (def2-TZVP).<sup>54</sup> Computation efficiency was improved by utilizing the resolution of identity (RI) approximation in conjunction with the appropriate auxiliary basis sets.<sup>55,56</sup> To ensure high-spin configurations for the Fe(III) centers, unrestricted geometry optimizations of the diferric species were performed on the high-spin (*i.e.*, ferromagnetic) state, which possesses an overall spin of 5. Atomic coordinates for the geometry-optimized models are provided in Tables S3–S6.<sup>†</sup>

The optimized structures were subsequently used to compute experimental properties for the diiron(II) dimers. These calculations employed the B3LYP functional<sup>57,58</sup> and def2-TZVP basis sets (unless otherwise noted). Auxiliary basis sets<sup>55</sup> were used to implement the resolution of identity and chain of sphere (RIJCOSX) approximation.<sup>59</sup> The role of solvent was accounted for using the conductor-like polarizable continuum model (C-PCM)<sup>60</sup> for acetonitrile. The antiferromagnetic ( $S = 0$ ) states were obtained by applying the broken-symmetry (BS) formalism, which yielded values of the exchange coupling constants ( $H_{\text{ex}} = -2JS_A \cdot S_B$  formalism).<sup>61,62</sup> The BS wavefunctions of the optimized structures were subsequently used for Mössbauer and time-dependent DFT (TD-DFT) calculations. Calculations of Mössbauer parameters applied a high resolution grid with an integration accuracy of 7.0 and CP(PPP) basis set<sup>63</sup> to the Fe atom. Isomer shifts ( $\delta$ ) were calculated from the linear correlation functions reported by Gordon *et al.* for nonheme iron species with mixed N/S ligation.<sup>28</sup> As in our previous study of **1** and **2**,<sup>44</sup> computed UV-vis absorption spectra were derived from TD-DFT calculations that employed the cam-B3LYP range-separated hybrid functional.<sup>64</sup> Absorption energies and intensities were computed for 40 excited states.<sup>65,66</sup> Plots of molecular orbitals and electron density difference maps were generated with the *ChemCraft* software program.

### III. Results and analysis

#### Formation of oxidized intermediates

Anaerobic solutions of the precursor complexes (**1** and **2**) are pale yellow due to the presence of thiolate-to-iron(II) charge transfer (CT) transitions in the near-UV region, yet rapid color changes are observed upon exposure to  $\text{O}_2$  at  $-40^\circ\text{C}$ . As shown in Fig. 1, addition of  $\text{O}_2$  to a solution of **1** in  $\text{CH}_3\text{CN}$  at  $-40^\circ\text{C}$  triggers immediate formation of a green chromophore (**3**) that displays an intense band at 598 nm. Similarly, the reaction of **2** with  $\text{O}_2$  yields a purple species (**4**) characterized by a peak at 524 nm and shoulder around 650 nm (Fig. 1, bottom). Assuming complete conversion, the dominant absorption features of **3** and **4** in the visible region possess molar absorptivities of roughly  $1000 \text{ M}^{-1} \text{ cm}^{-1}$  per Fe center. The same chromophores can be generated in  $\text{CH}_2\text{Cl}_2$  at low temperature

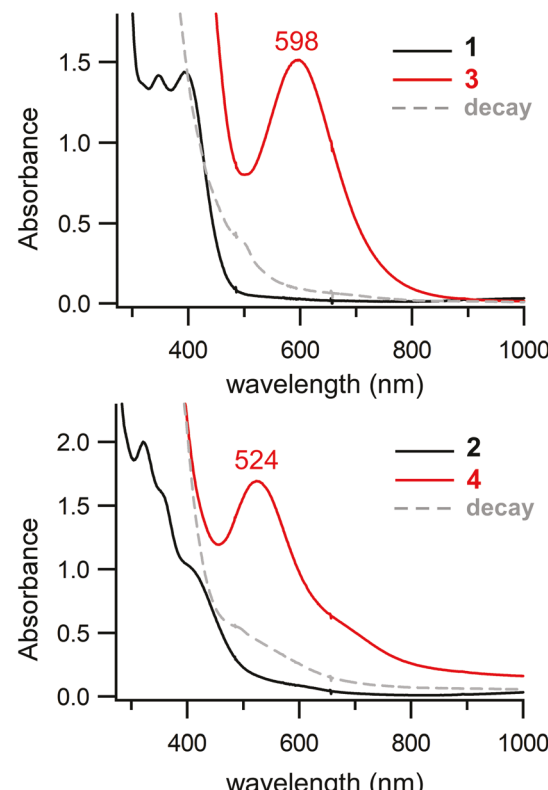


Fig. 1 UV-vis absorption spectra of the reaction of **1** (top) and **2** (bottom) with  $\text{O}_2$  in  $\text{CH}_3\text{CN}$  at  $-40^\circ\text{C}$ . Spectra of the Fe(II) precursors (**1** and **2**) and  $\text{O}_2$ -generated intermediates (**3** and **4**) are shown as black and red lines, respectively. The initial concentrations of **1** and **2** were 1.3 mM. The decay spectra (gray dashed lines) were obtained by warming solutions of **3** and **4** from  $-40^\circ\text{C}$  to room temperature.

( $-70^\circ\text{C}$ ). The lack of paramagnetically-shifted peaks in the  $^1\text{H}$  NMR spectra of **3** and **4** (Fig. S1<sup>†</sup>) indicate that these species are diamagnetic – a conclusion further supported by the variable-temperature Mössbauer experiments described in the next section.

Intermediates **3** and **4** are also generated, albeit in lower yields, upon addition of excess  $\text{H}_2\text{O}_2$  (10 equiv.) to the iron(II)-thiolate precursors in  $\text{CH}_3\text{CN}$  (Fig. S2<sup>†</sup>). Unlike the  $\text{O}_2$ -derived species, the chromophores generated with  $\text{H}_2\text{O}_2$  quickly decay even at  $-40^\circ\text{C}$  with half-lives of approximately 15 s. Interestingly, the characteristic absorption band of **4** also appears when **2** is treated with iodosylbenzene (PhIO; Fig. S3<sup>†</sup>), a well known oxo-transfer agent. Complex **1** is unreactive towards PhIO, perhaps owing to the greater steric bulk of the 2,4,6-trimethylthiophenolate ligand. The existence of these alternative routes eliminates the possibility that **3** and **4** are iron(III)-superoxide species.

For the sake of comparison, we sought to generate the iron(III)-thiolate analog of **2** through chemical one-electron oxidation. Treatment of **2** with one equivalent of ferrocenium cation,  $[\text{Fc}]^+$ , under anaerobic conditions yields a green species (**5**) with an absorption band at 630 nm (Fig. 2). The EPR spectrum of **5** features an axial  $S = 1/2$  signal ( $g_{\perp} = 2.16$ ,  $g_{\parallel} = 1.99$ ),

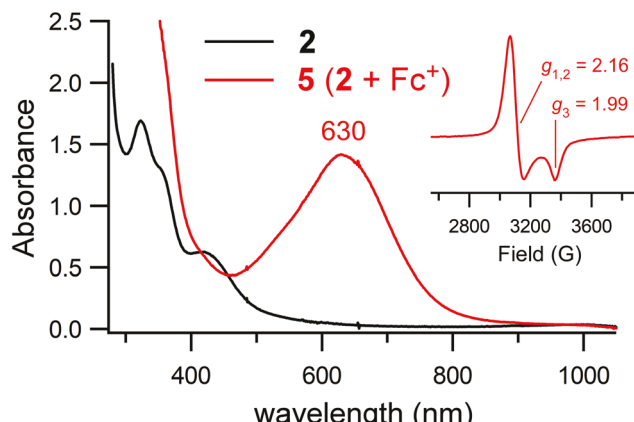


Fig. 2 UV-vis spectra of the oxidation of complex **2** (black line) to **5** (red line) via addition of one equivalent of  $[\text{Fc}]^{\text{PF}_6}$ . The reaction occurred in  $\text{CH}_3\text{CN}$  at  $-40\text{ }^{\circ}\text{C}$ . The initial concentration of **2** was  $0.90\text{ mM}$ . Inset: X-band EPR spectrum of **5** measured at  $10\text{ K}$  in frozen  $\text{CH}_3\text{CN}$ . Data were collected at a frequency of  $9.39\text{ GHz}$  and power of  $2.0\text{ mW}$ .

similar to those previously reported for low-spin iron(III)-thiolate complexes (Fig. 2, inset).<sup>67</sup> Given the sizable differences in their spectral features, it is clear that **4** and **5** are distinct species. Thus, we can conclude that the formation of **4** from its iron(II) precursor involves more than outer-sphere electron transfer to  $\text{O}_2$  (or  $\text{H}_2\text{O}_2$ ).

Intermediates **3** and **4** decay slowly at  $-40\text{ }^{\circ}\text{C}$  in  $\text{CH}_3\text{CN}$ , as indicated by the time traces shown in Fig. S4.<sup>†</sup> Warming the samples to room temperature also results in decay to products that lack distinctive absorption features (Fig. 1). Analysis of the reaction mixture with  $^1\text{H}$  NMR spectroscopy and GC-MS after work-up determined that, in both cases, the thiolate ligands are primarily converted to the corresponding disulfide products, consistent with our previous report.<sup>44</sup> Because some iron-oxo and -peroxy species are known to undergo reversible protonation,<sup>36,68</sup> we also examined the reactivity of **3** and **4** with weak acids like trifluoroacetic acid. However, the addition of acid always results in irreversible decay of the absorption features, yielding a spectrum similar to one observed at room temperature for the  $\text{O}_2$  reaction.

### Mössbauer spectroscopic studies

The electronic and magnetic properties of intermediates **3** and **4** were investigated with Mössbauer (MB) spectroscopy. MB samples were prepared as solutions in butyronitrile, as this solvent permitted the high concentrations ( $\sim 50\text{ mM}$ ) required for the study of complexes with only natural abundances of  $^{57}\text{Fe}$ . As reported in our earlier paper,<sup>44</sup> the precursor complexes (**1** and **2**) exhibit spectral components with isomer shifts ( $\delta$ ) above  $0.9\text{ mm s}^{-1}$  and large quadrupole splittings ( $\Delta E_Q > 2.8\text{ mm s}^{-1}$ ; see Fig. S5<sup>†</sup> for complex **2**). Exposure to  $\text{O}_2$  causes dramatic changes in the MB features consistent with oxidation of the iron center, although contributions from small amounts of the unreacted Fe(II) precursors are also evident. These Fe(II) features, accounting for 27% of the total

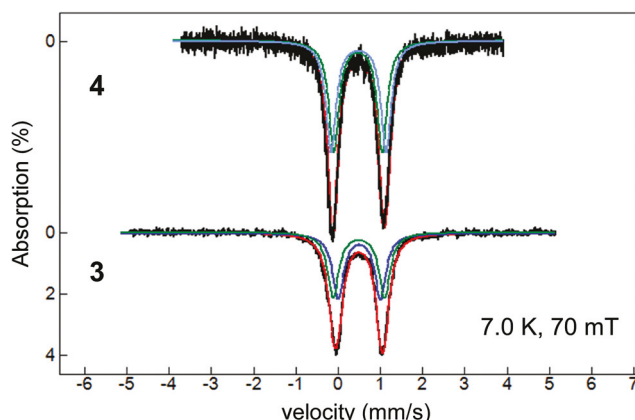
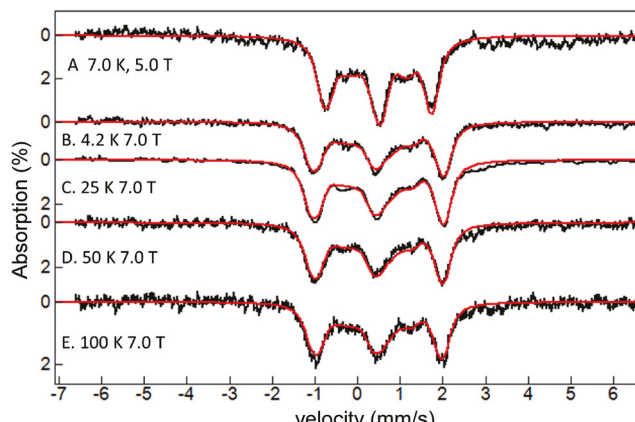


Fig. 3 Mössbauer spectra of complexes **3** and **4** measured at  $7.0\text{ K}$  and  $70\text{ mT}$ , prepared as described in the text. The hatch marks are the experimental data, and the colored lines are spectral fits generated with the parameters in Table 1. For clarity, both spectra were prepared by removing the unreacted Fe(II) species from the raw data.

iron in the sample of intermediate **3** and 8% of the total iron in the sample of intermediate **4** were removed by spectral subtraction, yielding the spectra shown in Fig. 3. The low-field MB spectra of **3** and **4** are quite similar, indicating that the complexes share the same electronic structure. In each case, the MB spectrum consists of a slightly asymmetric doublet that is comprised of two nearly identical quadrupole doublets in a  $1:1$  ratio. The  $1:1$  ratio of sub-components can be readily rationalized by assuming that **3** and **4** possess dimeric structures in which the coordination geometries of the Fe centers differ only slightly. The two sub-components of **3** have isomer shifts of  $0.47$  and  $0.49 \pm 0.02\text{ mm s}^{-1}$  and respective  $\Delta E_Q$  values of  $1.43$  and  $1.05\text{ mm s}^{-1}$ . Similar isomer shifts ( $\delta = 0.47$  and  $0.48 \pm 0.01\text{ mm s}^{-1}$ ) and quadrupole splittings ( $\Delta E_Q$  of  $1.14$  and  $1.30\text{ mm s}^{-1}$ ) were used in spectral fits of intermediate **4**. These MB parameters are characteristic of high-spin Fe(III) centers.<sup>69</sup> Moreover, the absence of broadenings or splittings in spectra measured at  $70\text{ mT}$  field (linewidths of  $0.3\text{ mm s}^{-1}$ ) is strongly indicative of diamagnetic ( $S = 0$ ) ground states, consistent with the presence of antiferromagnetic (AF) coupling between iron(III) centers in a dimeric structure.

Additional electronic-structure insights were obtained by collecting spectra in large applied magnetic fields (Fig. 4). These variable-field experiments were performed on samples of **4**, which possess smaller amounts of Fe(II) precursor than samples of **3**. The  $4.2\text{ K}$  spectrum of **4** at  $7.0\text{ Tesla}$  exhibits magnetic splittings that arise exclusively from the applied magnetic field, providing definitive evidence of a diamagnetic ground state. The strength of the AF coupling interaction was examined by simultaneous fitting of the variable-temperature series at  $7.0\text{ Tesla}$  between  $4.2$  and  $100\text{ K}$  with a model consisting of two coupled Fe(III) ions. This analysis found that the absolute value of the exchange coupling constant ( $J$ ) must be greater than  $60\text{ cm}^{-1}$  (using the  $H_{\text{ex}} = -2J \cdot S_A S_B$  formalism),



**Fig. 4** Variable-field, variable-temperature Mössbauer spectra of complex 4. The hatch marks are the experimental data, and the colored lines are spectral fits generated with the parameters in Table 1 as described in Experimental Methods.

indicative of strong AF exchange. This value is an estimate of the smallest  $|J|$ -value that would fit the temperature-dependent high-field data.

Mössbauer studies in the literature have revealed that  $J$ -values of diferric- $\mu$ -peroxy and  $\mu$ -hydroxo compounds are moderate to small for species that lack an additional monoatomic bridging group.<sup>70</sup> For example, Kitajima *et al.* reported a  $J$ -value of  $-33\text{ cm}^{-1}$  for  $[\text{Fe}_2^{\text{III}}(\mu\text{-O}_2)(\mu\text{-1,3-O}_2\text{CCH}_2\text{Ph})_2(\text{Tp}^{\text{IPr}2})]$  (where  $\text{Tp}^{\text{IPr}2}$  is a substituted trispyrazolylborate ligand).<sup>71</sup> The magnitude of  $J$  for this complex would likely be lower were it not for the two  $\mu$ -1,3-carboxylate ligands. DFT calculations by Goldberg and coworkers on a thiolate-ligated diferric- $\mu$ -peroxy complex without additional bridging ligands provided a small  $J$ -value of  $-5.5\text{ cm}^{-1}$ .<sup>32</sup> The magnitude of  $J$ -values for diiron (III)- $\mu$ -hydroxo complexes are similarly small, generally less than  $20\text{ cm}^{-1}$ .<sup>72,73</sup> In contrast, diferric complexes that possess a single oxo bridge generally exhibit large and negative exchange coupling constants ( $J < -80\text{ cm}^{-1}$ ).<sup>72</sup> Thus, the fact that  $J \leq -60\text{ cm}^{-1}$  for 4 supports the presence of an oxo bridge instead of a peroxo or hydroxo bridge.

### Resonance Raman spectroscopic studies

Additional insights into the geometric structures of 3 and 4 were gained through resonance Raman (rRaman) experiments. Concentrated samples were prepared in multiple solvents ( $\text{CH}_3\text{CN}$ ,  $\text{CD}_3\text{CN}$ ,  $\text{CD}_2\text{Cl}_2$ ) by treating the precursor complexes with  $^{16}\text{O}_2$  or  $^{18}\text{O}_2$ . Most spectra were collected at 77 K using 501.7 nm excitation with laser power of 20–30 mW; photo-decomposition was not observed under these conditions. As shown in Fig. 5, the spectrum of 4 in frozen  $\text{CH}_3\text{CN}$  exhibits an intense peak at  $820\text{ cm}^{-1}$  that shifts to  $777\text{ cm}^{-1}$  upon  $^{18}\text{O}_2$  substitution, as clearly evident in the  $^{16}\text{O}_2$ – $^{18}\text{O}_2$  difference spectrum. Intermediate 3 exhibits an analogous pair of isotopically-active peaks with energies of  $822\text{ cm}^{-1}$  and  $781\text{ cm}^{-1}$  ( $\Delta^{16}\text{O}/^{18}\text{O} = 41\text{ cm}^{-1}$ ; Fig. 5). The other observed features in the  $200$ – $1600\text{ cm}^{-1}$  region are insensitive to  $^{16}\text{O}_2$ – $^{18}\text{O}_2$  substitution.

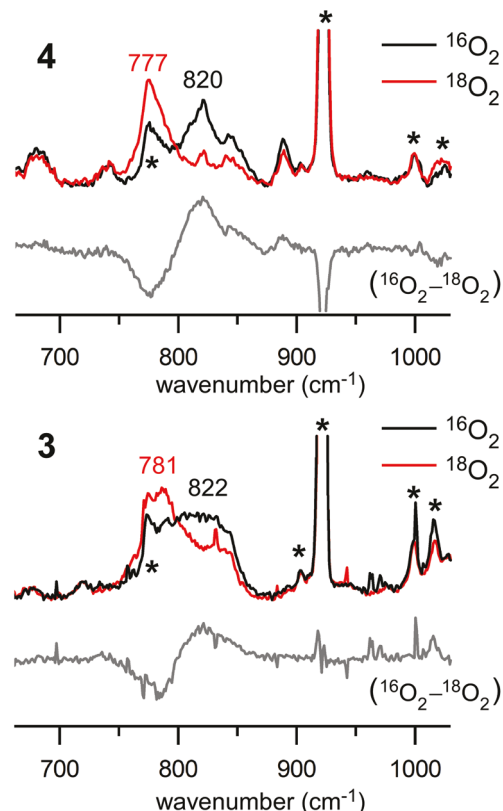


**Fig. 5** Resonance Raman spectra of 4 (top) and 3 (bottom) in frozen  $\text{CH}_3\text{CN}$  (77 K). Samples were prepared using either  $^{16}\text{O}_2$  (black lines) or  $^{18}\text{O}_2$  (red lines). Derivative-shaped features in the  $^{16}\text{O}_2$ – $^{18}\text{O}_2$  difference spectra (gray lines) are due to isotopically-active peaks. All spectra were measured using 501.7 nm laser excitation at a power of 20–30 mW at the sample. The solvent-derived features marked with an asterisk (\*) were used to normalize spectral intensities.

Samples of 4 generated with  $\text{H}_2\text{O}_2$  instead of  $\text{O}_2$  provide nearly identical spectra (Fig. S6†), and the peak near  $820\text{ cm}^{-1}$  down-shifts to  $782\text{ cm}^{-1}$  in samples prepared with  $^{18}\text{O}$ -substituted  $\text{H}_2\text{O}_2$  (Fig. S7†). These features disappear after warming and refreezing the sample, proving that the isotopically-active peak does not arise from a decay product. Therefore, we conclude that the structures of 3 and 4 contain one or more O-atoms derived from  $\text{O}_2$  (or  $\text{H}_2\text{O}_2$ ).

The observed frequencies and isotope shifts are suggestive of three possible core structures for 3 and 4: diiron(III)- $\mu$ -peroxy, diiron(III)- $\mu$ -oxo, and iron(IV)-oxo. The latter possibility (*i.e.*, mononuclear ferryl) can be ruled out based on the Mössbauer results, which demonstrated that these intermediates contain high-spin Fe(III) centers (*vide supra*). However, both diiron(III)- $\mu$ -peroxy and diiron(III)- $\mu$ -oxo structures are consistent with the rRaman data presented thus far. Diiron(III) complexes with  $\mu$ -1,2-peroxy ligands typically exhibit  $\nu(\text{O}-\text{O})$ -based modes with frequencies of  $800$ – $900\text{ cm}^{-1}$  and  $\Delta^{16}\text{O}/^{18}\text{O}$ -shifts of  $45$ – $50\text{ cm}^{-1}$ .<sup>32,70,74</sup> Similarly, the asymmetric Fe–O–Fe stretching mode ( $\nu_{\text{as}}$ ) of diiron(III)- $\mu$ -oxo species appears in the  $800$ – $900\text{ cm}^{-1}$  region, although the  $\Delta^{16}\text{O}/^{18}\text{O}$ -shifts tend to be smaller ( $30$ – $40\text{ cm}^{-1}$ ).<sup>41,75,76</sup> Previous studies have demon-

strated that the  $\nu_{as}(\text{Fe}-\text{O}-\text{Fe})$  frequency of diiron(III)- $\mu$ -oxo complexes increases as the Fe-O-Fe bond angle becomes more linear.<sup>76</sup>

In an effort to distinguish between the  $\mu$ -oxo and  $\mu$ -peroxo alternatives, rRaman samples of **4** were prepared using “scrambled”  $\text{O}_2$  that consists of a statistical mixture of  $^{16}\text{O}_2$ ,  $^{16}\text{O}^{18}\text{O}_2$ , and  $^{18}\text{O}_2$  in a roughly 1:2:1 ratio (see Experimental methods). As shown in Fig. 6, the rRaman spectrum of **4** generated with scrambled  $\text{O}_2$  exhibits peaks of equal intensity at 820 and 778  $\text{cm}^{-1}$ , matching the frequencies of peaks in the  $^{16}\text{O}_2$  and  $^{18}\text{O}_2$  spectra, respectively. Indeed, this spectrum (C in Fig. 6) is nearly identical to the one obtained by digital averaging of the  $^{16}\text{O}_2$  and  $^{18}\text{O}_2$  spectrum (gray line in Fig. 6). This result demonstrates that the sample of **4** generated with scrambled  $\text{O}_2$  contains only two isotopomers,  $\text{Fe}^{16}\text{O}-\text{Fe}$  and  $\text{Fe}^{18}\text{O}-\text{Fe}$ , in equal amounts. In contrast, a symmetric diiron (III)- $\mu$ -peroxo species would be expected to display three  $\nu(\text{O}-\text{O})$  peaks arising from the three possible isotopomers; in this case, the most intense feature would possess an intermediate frequency of  $\sim 800 \text{ cm}^{-1}$ . The absence of a  $\nu(\text{O}^{16}\text{O}-\text{O}^{18}\text{O})$  peak at this frequency in spectrum C, therefore, is inconsistent with a  $\mu$ -peroxo structure. Instead, the rRaman data in Fig. 6 confirm the presence of an Fe-O-Fe unit in **4** (and, by extension, the analogous intermediate **3**).

Intermediates **3** and **4** also exhibit multiple intense rRaman peaks in the 320–410  $\text{cm}^{-1}$  region (Fig. 7) that are insensitive to isotopic substitution of  $\text{O}_2$ . Based on literature precedents, these features are assigned to vibrational modes that possess dominant  $\nu(\text{Fe}-\text{S})$  stretching character,<sup>32,67</sup> along with contributions from  $\nu(\text{S}-\text{C})$  stretching and  $\delta(\text{S}-\text{C}-\text{C})$  bending motions due to kinematic coupling.<sup>77</sup> The presence of  $\nu(\text{Fe}-\text{S})$  features confirms that the thiolate ligands remain coordinated in a monodentate fashion in **3** and **4**. The peaks at 321 and 403  $\text{cm}^{-1}$  in the spectrum of **3** gain significant intensity (relative to solvent) as the laser excitation wavelength moves from 501.7 nm to 647.1 nm (Fig. S8†). Interestingly, the opposite

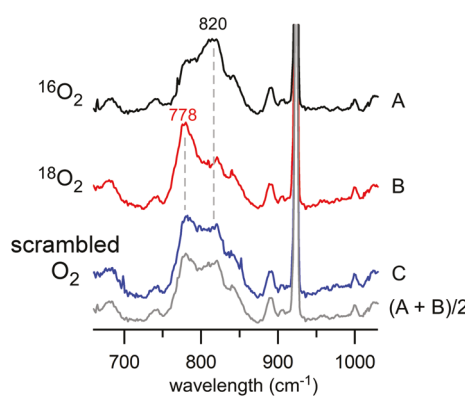


Fig. 6 Resonance Raman spectra of **4** in frozen  $\text{CH}_3\text{CN}$  collected using 501.7 nm excitation (24–30 mW at sample). The samples were prepared by treating 10 mM solutions of **2** with  $^{16}\text{O}_2$  (A, black line),  $^{18}\text{O}_2$  (B, red line), or scrambled  $\text{O}_2$  (C, blue line). The bottom spectrum (gray line), generated by digital addition, is half the sum of spectra A and B. Solvent-derived peaks were used to normalize spectral intensities.

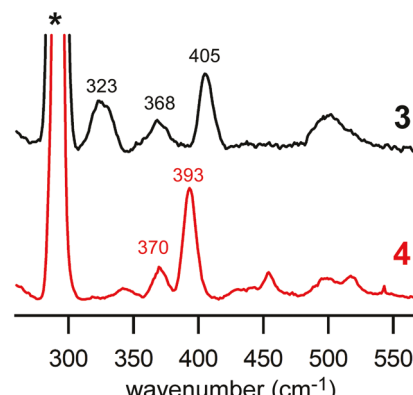
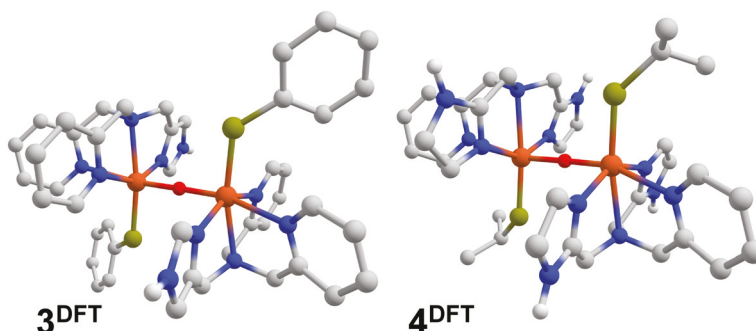


Fig. 7 Resonance Raman spectra of **3** and **4** in frozen  $\text{CD}_2\text{Cl}_2$  (77 K). Spectra were collected with laser excitation of 514.5 nm (**3**) and 501.7 nm (**4**). Samples were prepared by addition of  $\text{O}_2$  to solutions of the precursor complexes. The solvent-derived peak marked with an asterisk (\*) was used to normalize spectral intensities.

trend is observed for the  $\nu_{as}(\text{Fe}-\text{O}-\text{Fe})$ -based peak at 822  $\text{cm}^{-1}$ . The results suggest that the broad absorption manifolds of **3** and **4** in the visible region (Fig. 1) are composed of multiple bands with varying degrees of  $\text{S} \rightarrow \text{Fe}(\text{III})$  and  $\text{O} \rightarrow \text{Fe}(\text{III})$  charge transfer (CT) character. The nature of these CT transitions is further examined by computational methods in the next section.

### Density functional theory calculations

Due to the instability of **3** and **4** at temperatures above  $-30^\circ\text{C}$ , it was not possible to grow suitable crystals for crystallographic studies; therefore, DFT geometry optimizations were employed to generate structural models of these intermediates. Following the conclusions of our spectroscopic studies (*vide supra*), we created truncated models of **3** and **4** (labeled **3**<sup>DFT</sup> and **4**<sup>DFT</sup>, respectively) that possess an unsupported  $[\text{Fe}_2^{\text{III}}(\mu-\text{O})]^{4+}$  core. The analogous  $\mu$ -1,2-peroxo models (**P1** and **P2**) were also examined for the sake of comparison. Energy-minimized structures of **3**<sup>DFT</sup> and **4**<sup>DFT</sup> are shown in Fig. 8 and metric parameters for all computational models are summarized in Table S1.† In these dimeric structures, the two  $\text{Fe}(\text{III})$  centers exist in symmetric coordination environments with nearly identical sets of Fe-N/O/S bond distances and angles. Each model possesses a quasi-inversion center due to the *anti* conformation of the thiolate ligands and  $\text{L}^{\text{A}/\text{B}}$  chelates (Fig. 8). The  $[\text{Fe}_2^{\text{III}}(\mu-\text{O})]^{4+}$  cores of **3**<sup>DFT</sup> and **4**<sup>DFT</sup> are nearly linear with Fe-O-Fe bond angles of  $178^\circ$  and  $175^\circ$ , respectively, and Fe-O bond distances of 1.87  $\text{\AA}$ , resulting in Fe-Fe separations of  $\sim 3.74 \text{ \AA}$ . The  $\mu$ -1,2-peroxo models (**P1** and **P2**) exhibit larger Fe-Fe distances of  $\sim 4.75 \text{ \AA}$ . The computed Fe-S bond distances for all models lie within a narrow range of  $2.31 \pm 0.03 \text{ \AA}$ , consistent with previously published crystal structures of related complexes.<sup>36,38,41</sup> The Fe-N distances exhibit greater variability due to elongations caused by the *trans* influence of the anionic thiolate and (per)oxo donors (Table S1†).



**Fig. 8** DFT geometry-optimized models of intermediates **3** and **4**. Most hydrogen atoms are omitted for the sake of clarity. The thiolate ligands have been modified as described in Computational Methods. Atomic colors: C, gray; N, blue; O, red; S, yellow; Fe, orange.

Broken-symmetry DFT calculations confirmed that the two high-spin Fe(III) centers of each model are antiferromagnetically coupled to yield a diamagnetic ground state. These calculations provided exchange coupling constants ( $J$ ) of  $-82$  and  $-78\text{ cm}^{-1}$  for **3**<sup>DFT</sup> and **4**<sup>DFT</sup>, respectively (the  $H_{\text{ex}} = -2J \cdot S_{\text{ASB}}$  formalism and Yamaguchi method were employed). The computed values are broadly consistent with the variable-temperature and  $\gamma$ -field Mössbauer data, which estimated that  $J \leq -60\text{ cm}^{-1}$  for **4**. The strong AF interaction is mediated by the monoatomic  $\mu$ -oxo bridge. The computed  $J$ -values for **P1** and **P2**, while still negative, have much smaller magnitudes of  $-14$  and  $-11$ , respectively. These results are consistent with prior studies that demonstrated that  $\mu$ -oxo ligands are better mediators of AF exchange than  $\mu$ -1,2-peroxo ligands.<sup>70,72</sup>

The DFT-computed Mössbauer parameters ( $\delta$  and  $\Delta E_Q$ ) are listed in Table 1. The good agreement between the experimental and computed values, especially with respect to isomer shifts, provides further evidence that **3** and **4** are symmetric diferric intermediates. As expected, the computed MB parameters are quite similar for the  $\mu$ -oxo and  $\mu$ -peroxo models, although the  $\delta$ - and  $\Delta E_Q$ -values are slightly larger for **P1** and **P2**. Thus, our DFT results suggest that zero-field MB spectroscopy, by itself, is not an effective method for identifying the bridging ligand of diferric complexes.

The origins of the intense UV-vis features of **3** and **4** were elucidated by time-dependent DFT (TD-DFT) calculations. The excellent agreement between the computed and experimental absorption spectra, as shown in Fig. 9, further supports the veracity of our DFT models. Like the experimental data, the TD-DFT spectra consist of a single dominant band in the

visible region that is red-shifted in **3** compared to **4** ( $\lambda_{\text{max}}(3) > \lambda_{\text{max}}(4)$ ). The electron-density difference maps (EDDMs; inset of Fig. 9) reveal that these bands arise from  $S(\pi) \rightarrow \text{Fe(III)}$  CT bands. The  $S(\pi)$  donor orbitals are oriented perpendicular to the Fe-S bond axes. Higher-energy bands in the near UV-region possess a mixture of  $\text{oxo}(\pi) \rightarrow \text{Fe(III)}$  and  $S(\sigma) \rightarrow \text{Fe(III)}$  CT character. These results are fully consistent with the observed rRaman enhancement of  $\nu(\text{Fe-S})$  and  $\nu_{\text{as}}(\text{Fe-O-Fe})$  modes at longer and shorter excitation wavelengths, respectively (*vide supra*). The TD-DFT computed spectrum of the hypothetical **P2** model is quite distinct from those generated for the diiron(III)- $\mu$ -oxo models. The **P2** spectrum features an intense near-IR band ( $\lambda_{\text{max}} \sim 970\text{ nm}$ ) that arises from a peroxo-to-Fe(III) CT transition, in addition to multiple  $S \rightarrow \text{Fe(III)}$  CT bands in the  $400\text{--}600\text{ nm}$  region (Fig. S9†). This general pattern of absorption bands resembles the experimental spectrum reported by Gordon *et al.* for a thiolate-ligated diiron(III)- $\mu$ -peroxo dimer.<sup>32</sup> These results suggest that  $\mu$ -oxo and  $\mu$ -peroxo diferric structures can be reliably distinguished by major differences in their UV-vis absorption features.

#### IV. Discussion and conclusions

Two mononuclear iron(II)-thiolate complexes (**1** and **2**), which represent active-site models of nonheme iron sulfoxide synthases, react with  $\text{O}_2$  at low temperatures ( $< -40\text{ }^{\circ}\text{C}$ ) to yield metastable species (**3** and **4**, respectively). Multiple spectroscopic techniques, namely UV-vis absorption, VTVH-MB, and rRaman, were required to uncover the identities of **3** and **4**.

**Table 1** Experimental and DFT-computed Mössbauer parameters for intermediates **3** and **4**

Experimental MB parameters					DFT-computed MB parameters			
Int	Species	$\delta$ (mm s $^{-1}$ )	$\Delta E_Q$ (mm s $^{-1}$ )	FWHM (mm s $^{-1}$ )	Model	Site	$\delta$ (mm s $^{-1}$ )	$ \Delta E_Q $ (mm s $^{-1}$ )
<b>3</b>	<i>Sp1</i> (50%)	0.47(2)	1.43(2)	0.30	<b>3</b> <sup>DFT</sup>	Fe1	0.537	0.775
	<i>Sp2</i> (50%)	0.49(2)	1.05(2)	0.30		Fe2	0.534	0.727
<b>4</b>	<i>Sp1</i> (50%)	0.47(1)	1.14(1)	0.28	<b>4</b> <sup>DFT</sup>	Fe1	0.545	0.735
	<i>Sp2</i> (50%)	0.48(1)	1.30(1)	0.28		Fe2	0.546	0.734

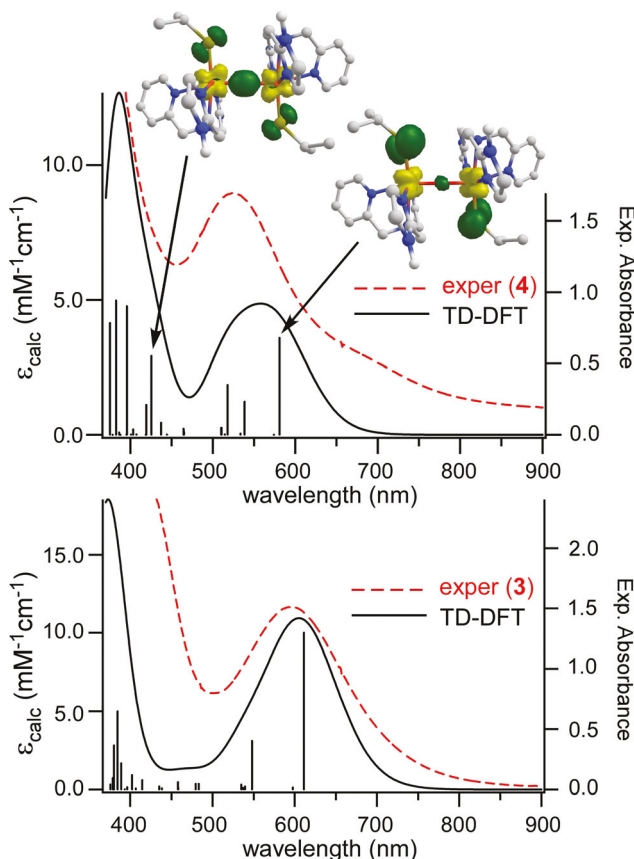
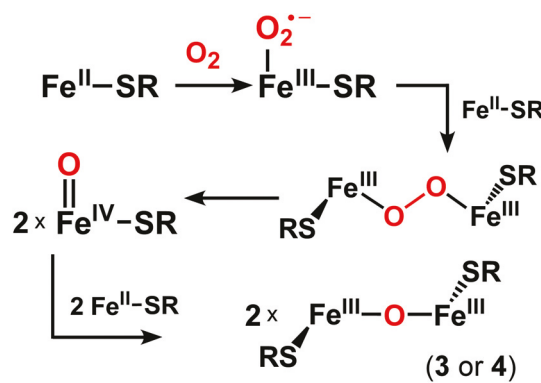


**Fig. 9** TD-DFT computed absorption spectra (solid black lines) of intermediates **4** (top) and **3** (bottom). The black sticks correspond to the energies and intensities of computed transitions. The TD-DFT spectra are compared to experimental spectra (dashed red lines) measured in  $\text{CH}_3\text{CN}$  at  $-40^\circ\text{C}$  (initial Fe concentration of 1.3 mM). The inset displays electron density difference maps for two intense transitions in the computed spectrum of **4**. The green and yellow areas represent the loss and gain, respectively, of electron density during the excitation.

Mössbauer studies revealed that both intermediates possess high-spin Fe(III) centers and diamagnetic ( $S = 0$ ) ground-states, indicative of dimeric structures in which the ferric ions are coupled to each other antiferromagnetically. The AF coupling interaction is quite strong, as MB spectra of **4** measured at elevated temperature (100 K) and high magnetic field lack contributions from paramagnetic excited states (Fig. 4). Insights into the geometric structures of **3** and **4** were primarily gained through rRaman studies involving different isotopes of  $\text{O}_2$ . Both species exhibit an isotopically-active peak near  $820\text{ cm}^{-1}$  that downshifts by  $\sim 42\text{ cm}^{-1}$  upon  $^{18}\text{O}_2$  substitution (Fig. 5), consistent with either diiron- $\mu$ -oxo or - $\mu$ -peroxy structures. To distinguish between these two possibilities, rRaman samples of **4** were prepared with a statistical mixture of  $^{16}\text{O}_2$ ,  $^{16}\text{O}^{18}\text{O}$ , and  $^{18}\text{O}_2$ . The resulting spectra revealed the presence of two isotopomers (Fig. 6), providing definitive proof that these intermediates possess a diiron(III)- $\mu$ -oxo core. As this study highlights, MB and rRaman spectroscopies provide complementary insights that are highly effective in elucidating the

geometric and electronic structures of Fe/ $\text{O}_2$  intermediates, particularly in cases of diamagnetic or integer-spin species that are inaccessible by EPR. Structural models of **3** and **4** obtained through DFT methods provided calculated MB parameters and TD-DFT absorption spectra consistent with the experimental data. The computational results indicate that the intense absorption features of **3** and **4** in the visible region arise from  $\text{S} \rightarrow \text{Fe(III)}$  and  $\text{O} \rightarrow \text{Fe(III)}$  CT transitions.

Following the  $\text{O}_2$  activation mechanisms proposed for related complexes, it is likely that the formation of **3** and **4** proceeds *via* an unobserved diiron(III)-peroxy species, as illustrated in Scheme 3. Homolytic O-O bond cleavage then generates putative oxoiron(IV) intermediates, which react with a second equivalent of the Fe(II) precursor to yield a diiron(III)- $\mu$ -oxo unit. This mechanism is consistent with the fact that **3** and **4** are also generated by reaction of the precursor complexes with  $\text{H}_2\text{O}_2$  (Fig. S2†). It is also significant that intermediate **4** can also be prepared by treatment of **2** with PhIO – an O-atom transfer agent. This reaction likely proceeds *via* an unobserved oxoiron(IV) species that subsequently combines with a second Fe(II) equivalent, as illustrated in Fig. S10.† The viability of the PhIO route is further evidence that these intermediates possess  $\mu$ -oxo (as opposed to  $\mu$ -peroxy) cores, as the oxidant in this case lacks an O-O bond. Another possible mechanism, as reported by Duboc and coworkers,<sup>41</sup> involves dismutation of the two diiron(III)- $\mu$ -peroxy intermediates to yield the two diiron(III)- $\mu$ -oxo cores and  $\text{O}_2$ . Regardless of pathway, formation of **3** and **4** using  $\text{O}_2$  proceeds through an unobserved diiron(III)- $\mu$ -peroxy species. Indeed, diiron(III)-oxo and -peroxy intermediates often coexist on the same reaction profile, and it can be challenging to distinguish such species due to close similarities in their zero-field Mössbauer parameters ( $\delta$ ,  $\Delta E_Q$  values) and rRaman features. The present study has sought to clearly define the spectroscopic signatures of thiolate-ligated diiron(III)-oxo complexes and provide guidelines for identifying intermediates derived from the reaction of Fe(II) complexes and  $\text{O}_2$ . In particular, we have demonstrated that the study of rRaman samples prepared with scrambled  $\text{O}_2$  offers an effective way to distinguish between  $\mu$ -oxo and  $\mu$ -



**Scheme 3** Proposed mechanism for formation of intermediates **3** and **4**.

peroxyo alternatives. Furthermore, the latter often display extreme photosensitivity upon laser irradiation,<sup>32,78</sup> whereas  $\mu$ -oxo species are resistant to photo-decomposition in our experience. Strong AF exchange coupling interactions, as indicated by  $J$ -values more negative than  $-50\text{ cm}^{-1}$ , are also characteristic of diiron(III)- $\mu$ -oxo species. Finally, the UV-vis absorption spectra of **3** and **4** (Fig. 1) feature a dominant  $\text{S} \rightarrow \text{Fe(III)}$  band in the 450–600 nm region, similar to previously-reported thiolate-ligated diiron(III)-oxo complexes.<sup>36,38,41</sup> Kovacs *et al.* have demonstrated that the  $\lambda_{\text{max}}$  value of this feature is linearly correlated with the  $\text{Fe}^{3+/2+}$  oxidation potential.<sup>38</sup> In contrast, unsupported diiron(III)- $\mu$ -peroxyo complexes typically exhibit multiple absorption bands across the visible region, including a band at longer wavelength ( $\lambda_{\text{max}} > 600\text{ nm}$ ) that arises from a peroxyo-to-Fe(III) transition.<sup>70</sup> Thus, UV-vis absorption spectroscopy can corroborate the presence of an oxo or peroxy bridge for diiron(III) complexes.

It was not possible to grow X-ray quality crystals of **3** and **4** due to their instability even at low temperatures. Thus, it was necessary to employ DFT geometry optimizations to obtain the structural models shown in Fig. 8. The instability of **3** and **4** is likely due to the presence of monodentate thiolate ligands that facilitate the observed decay to disulfide products. In most previous reports of thiolate-ligated diiron(III)- $\mu$ -oxo complexes, the S-donor is appended to a multidentate ligand framework and the complex is stable enough for crystallization. The Kovacs group recently reported the X-ray structures of four diiron(III)- $\mu$ -oxo complexes in which the alkyl thiolate donors are incorporated into pentadentate  $\text{N}_4\text{S}$  chelates.<sup>38</sup> Table S2† compares relevant metric parameters for the computed and experimental structures. In addition, the Duboc and Daresbourg groups have published X-ray structures of diiron(III)- $\mu$ -oxo complexes capped by tetradentate  $\text{N}_2\text{S}_2$  ligands, resulting in five-coordinate Fe geometries.<sup>35,41</sup> Most of these crystallographic structures feature nearly linear Fe–O–Fe units similar to the DFT-generated models of **3** and **4**, although the Duboc structure exhibits a bent Fe–O–Fe angle of  $145^\circ$ . The computed Fe–O bond distances of  $1.87\text{ \AA}$  in **3**<sup>DFT</sup> and **4**<sup>DFT</sup> are slightly longer than those observed crystallographically, which typically range between  $1.77$  and  $1.81\text{ \AA}$ . In the DFT models, the Fe–N bonds *trans* to the anionic thiolate and oxo donors are lengthened to distances of  $2.35$ – $2.47\text{ \AA}$  (Table S1†). Similarly long Fe–N bond distances have been observed in experimental structures of thiolate-ligated diiron(III)- $\mu$ -oxo complexes.<sup>38,40,79</sup>

The  $\text{O}_2$  reactivity of **1** and **2**, as described here, underscores the challenges involved in the development of functional models of sulfoxide synthases, such as EgtB and OvoA. The enzymes avoid non-productive pathways by sequestering the nonheme Fe center within the active-site pocket, thereby avoiding the formation of diferric- $\mu$ -oxo structures and disulfide byproducts observed for our model complexes. Second-sphere residues within the active site are also essential for directing the catalytic intermediates towards S–C bond formation instead of S-dioxygenation. Thus, successful efforts to generate functional SO synthase models will likely require more

complex chelates that incorporate outer-sphere donors and/or isolation the iron center within a supramolecular structure.

## Conflicts of interest

There are no conflicts of interest to declare.

## Acknowledgements

Financial support was provided by the National Institutes of Health (GM126522 to A. T. F. and GM117120 to J. R. M.). We are grateful to Dr Thomas Brunold (University of Wisconsin) for access to resonance Raman instrumentation. We thank Drs James Kincaid and Remigio Usai for assistance in preparing samples with scrambled  $\text{O}_2$ . The Mössbauer experiments were supported by start-up funds from The College of Arts and Sciences (C. V. P.) and the Undergraduate Research Opportunities Program (A. L. P.) at the University of St. Thomas. C. V. P. is grateful to Drs Yisong Guo and Jin Xiong (Carnegie Mellon University) for recording high-field Mössbauer data and to Dr Michael Hendrich (Carnegie Mellon University) for the gift of the program *Spincount*. TD-DFT calculations were performed on the Raj Cluster at Marquette University, which was built with funds from the National Science Foundation (CNS-1828649). Upgrades to the EPR spectrometer at UW-Madison were funded by the National Science Foundation (CHE-0741901).

## References

- 1 I. G. Denisov, T. M. Makris, S. G. Sligar and I. Schlichting, *Chem. Rev.*, 2005, **105**, 2253–2278.
- 2 T. H. Yosca, J. Rittle, C. M. Krest, E. L. Onderko, A. Silakov, J. C. Calixto, R. K. Behan and M. T. Green, *Science*, 2013, **342**, 825–829.
- 3 T. H. Yosca, A. P. Ledray, J. Ngo and M. T. Green, *J. Biol. Inorg. Chem.*, 2017, **22**, 209–220.
- 4 J. T. Groves, *Nat. Chem.*, 2014, **6**, 89–91.
- 5 A. P. Yeh, Y. Hu, F. E. Jenney Jr., M. W. W. Adams and D. C. Rees, *Biochemistry*, 2000, **39**, 2499–2508.
- 6 J. A. Kovacs and L. M. Brines, *Acc. Chem. Res.*, 2007, **40**, 501–509.
- 7 M. D. Clay, F. E. Jenney Jr., P. L. Hagedoorn, G. N. George, M. W. W. Adams and M. K. Johnson, *J. Am. Chem. Soc.*, 2002, **124**, 788–805.
- 8 L. M. Brines and J. A. Kovacs, *Eur. J. Inorg. Chem.*, 2007, 29–38.
- 9 P. L. Roach, I. J. Clifton, C. M. Hensgen, N. Shibata, C. J. Schofield, J. Hajdu and J. E. Baldwin, *Nature*, 1997, **387**, 827–830.
- 10 J. G. McCoy, L. J. Bailey, E. Bitto, C. A. Bingman, D. J. Aceti, B. G. Fox and G. N. Phillips Jr., *Proc. Natl. Acad. Sci. U. S. A.*, 2006, **103**, 3084–3089.
- 11 C. M. Driggers, S. J. Hartman and P. A. Karplus, *Protein Sci.*, 2015, **24**, 154–161.

12 C. M. Driggers, K. M. Kean, L. L. Hirschberger, R. B. Cooley, M. H. Stipanuk and P. A. Karplus, *J. Mol. Biol.*, 2016, **428**, 3999–4012.

13 K. V. Goncharenko, A. Vit, W. Blankenfeldt and F. P. Seebeck, *Angew. Chem., Int. Ed.*, 2015, **54**, 2821–2824.

14 N. Naowarojna, S. Irani, W. Hu, R. Cheng, L. Zhang, X. Li, J. Chen, Y. J. Zhang and P. Liu, *ACS Catal.*, 2019, **9**, 6955–6961.

15 I. Pettinati, J. Brem, M. A. McDonough and C. J. Schofield, *Hum. Mol. Genet.*, 2015, **24**, 2458–2469.

16 S. Goudarzi, J. T. Babicz, O. Kabil, R. Banerjee and E. I. Solomon, *J. Am. Chem. Soc.*, 2018, **140**, 14896–14911.

17 E. I. Solomon, S. Goudarzi and K. D. Sutherlin, *Biochemistry*, 2016, **55**, 6363–6374.

18 S. Aluri and S. P. De Visser, *J. Am. Chem. Soc.*, 2007, **129**, 14846–14847.

19 A. S. Faponle, F. P. Seebeck and S. P. de Visser, *J. Am. Chem. Soc.*, 2017, **139**, 9259–9270.

20 A. R. Stampfli and F. P. Seebeck, *Curr. Opin. Chem. Biol.*, 2020, **59**, 111–118.

21 E. Tamanaha, B. Zhang, Y. Guo, W.-C. Chang, E. W. Barr, G. Xing, J. St. Clair, S. Ye, F. Neese, J. M. Bollinger and C. Krebs, *J. Am. Chem. Soc.*, 2016, **138**, 8862–8874.

22 E. P. Tchesnokov, A. S. Faponle, C. G. Davies, M. G. Quesne, R. Turner, M. Fellner, R. J. Souness, S. M. Wilbanks, S. P. de Visser and G. N. L. Jameson, *Chem. Commun.*, 2016, **52**, 8814–8817.

23 A. C. McQuilken and D. P. Goldberg, *Dalton Trans.*, 2012, **41**, 10883–10899.

24 J. A. Kovacs, *Chem. Rev.*, 2004, **104**, 825–848.

25 M. Sallmann, I. Siewert, L. Fohlmeister, C. Limberg and C. Knispel, *Angew. Chem., Int. Ed.*, 2012, **51**, 2234–2237.

26 M. Sallmann, B. Braun and C. Limberg, *Chem. Commun.*, 2015, **51**, 6785–6787.

27 A. C. McQuilken, Y. Jiang, M. A. Siegler and D. P. Goldberg, *J. Am. Chem. Soc.*, 2012, **134**, 8758–8761.

28 J. B. Gordon, J. P. McGale, J. R. Prendergast, Z. Shirani-Sarmazeh, M. A. Siegler, G. N. L. Jameson and D. P. Goldberg, *J. Am. Chem. Soc.*, 2018, **140**, 14807–14822.

29 A. A. Fischer, N. Stracey, S. V. Lindeman, T. C. Brunold and A. T. Fiedler, *Inorg. Chem.*, 2016, **55**, 11839–11853.

30 A. A. Fischer, S. V. Lindeman and A. T. Fiedler, *Chem. Commun.*, 2018, **54**, 11344–11347.

31 M. N. Blakely, M. A. Dedushko, P. C. Y. Poon, G. Villar-Acevedo and J. A. Kovacs, *J. Am. Chem. Soc.*, 2019, **141**, 1867–1870.

32 J. B. Gordon, A. C. Vilbert, I. M. DiMucci, S. N. MacMillan, K. M. Lancaster, P. Moenne-Loccoz and D. P. Goldberg, *J. Am. Chem. Soc.*, 2019, **141**, 17533–17547.

33 J. Shearer, R. C. Scarrow and J. A. Kovacs, *J. Am. Chem. Soc.*, 2002, **124**, 11709–11717.

34 R. M. Theisen and J. A. Kovacs, *Inorg. Chem.*, 2005, **44**, 1169–1171.

35 G. Musie, C.-H. Lai, J. H. Reibenspies, L. W. Sumner and M. Y. Dahrensborg, *Inorg. Chem.*, 1998, **37**, 4086–4093.

36 R. M. Theisen, J. Shearer, W. Kaminsky and J. A. Kovacs, *Inorg. Chem.*, 2004, **43**, 7682–7690.

37 S. Ohta, S. Yokozawa, Y. Ohki and K. Tatsumi, *Inorg. Chem.*, 2012, **51**, 2645–2651.

38 S. Toledo, P. C. Y. Poon, M. Gleaves, J. Rees, D. M. Rogers, W. Kaminsky and J. A. Kovacs, *Inorg. Chim. Acta*, 2021, **524**, 120422.

39 P. Karsten and J. Strahle, *Acta Crystallogr., Sect. C: Cryst. Struct. Commun.*, 1999, **55**, 488–489.

40 S. C. Davies, D. L. Hughes, R. L. Richards and J. R. Sanders, *J. Chem. Soc., Dalton Trans.*, 2002, 1442–1447.

41 L. Wang, M. Gennari, F. G. Cantu Reinhard, S. K. Padamati, C. Philouze, D. Flot, S. Demeshko, W. R. Browne, F. Meyer, S. P. de Visser and C. Duboc, *Inorg. Chem.*, 2020, **59**, 3249–3259.

42 M. Gennari and C. Duboc, *Acc. Chem. Res.*, 2020, **53**, 2753–2761.

43 L. Wang, M. Gennari, F. G. Cantu Reinhard, J. Gutierrez, A. Morozan, C. Philouze, S. Demeshko, V. Artero, F. Meyer, S. P. de Visser and C. Duboc, *J. Am. Chem. Soc.*, 2019, **141**, 8244–8253.

44 D. M. Ekanayake, A. A. Fischer, M. E. Elwood, A. M. Guzek, S. V. Lindeman, C. V. Popescu and A. T. Fiedler, *Dalton Trans.*, 2020, **49**, 17745–17757.

45 H. Song, A. S. Her, F. Raso, Z. Zhen, Y. Huo and P. Liu, *Org. Lett.*, 2014, **16**, 2122–2125.

46 H. Song, M. Leninger, N. Lee and P. Liu, *Org. Lett.*, 2013, **15**, 4854–4857.

47 A. R. Stampfli, K. V. Goncharenko, M. Meury, B. N. Dubey, T. Schirmer and F. P. Seebeck, *J. Am. Chem. Soc.*, 2019, **141**, 5275–5285.

48 A. R. Stampfli, W. Blankenfeldt and F. P. Seebeck, *Curr. Opin. Struct. Biol.*, 2020, **65**, 1–8.

49 L. M. Proniewicz, A. Bruha, K. Nakamoto, E. Kyuno and J. R. Kincaid, *J. Am. Chem. Soc.*, 1989, **111**, 7050–7056.

50 F. Neese, *ORCA - An Ab Initio, DFT and Semiempirical Electronic Structure Package, version 4.0*, Max Planck Institute for Chemical Energy Conversion, Muelheim (Germany), 2017.

51 F. Neese, *Wiley Interdiscip. Rev.: Comput. Mol. Sci.*, 2012, **2**, 73–78.

52 A. D. Becke, *J. Chem. Phys.*, 1986, **84**, 4524–4529.

53 J. P. Perdew, *Phys. Rev. B: Condens. Matter Mater. Phys.*, 1986, **33**, 8822–8824.

54 F. Weigend and R. Ahlrichs, *Phys. Chem. Chem. Phys.*, 2005, **7**, 3297–3305.

55 F. Weigend, *Phys. Chem. Chem. Phys.*, 2006, **8**, 1057–1065.

56 F. Weigend, *J. Comput. Chem.*, 2008, **29**, 167–175.

57 A. D. Becke, *J. Chem. Phys.*, 1993, **98**, 5648–5652.

58 C. T. Lee, W. T. Yang and R. G. Parr, *Phys. Rev. B: Condens. Matter Mater. Phys.*, 1988, **37**, 785–789.

59 F. Neese, F. Wennmohs, A. Hansen and U. Becker, *Chem. Phys.*, 2009, **356**, 98–109.

60 V. Barone and M. Cossi, *J. Phys. Chem. A*, 1998, **102**, 1995–2001.

61 L. Noddeman, *J. Chem. Phys.*, 1981, **74**, 5737–5743.

62 S. Sinnecker, F. Neese, L. Noddleman and W. Lubitz, *J. Am. Chem. Soc.*, 2004, **126**, 2613–2622.

63 The “core properties” basis set is derived from the TurboMole DZ basis set developed by Ahlrichs and coworkers.

64 T. Yanai, D. P. Tew and N. C. Handy, *Chem. Phys. Lett.*, 2004, **393**, 51–57.

65 S. Hirata and M. Head-Gordon, *Chem. Phys. Lett.*, 1999, **314**, 291–299.

66 S. Hirata and M. Head-Gordon, *Chem. Phys. Lett.*, 1999, **302**, 375–382.

67 A. A. Fischer, J. R. Miller, R. J. Jodts, D. M. Ekanayake, S. V. Lindeman, T. C. Brunold and A. T. Fiedler, *Inorg. Chem.*, 2019, **58**, 16487–16499.

68 G. Roelfes, V. Vrajmasu, K. Chen, R. Y. N. Ho, J.-U. Rohde, C. Zondervan, R. M. la Crois, E. P. Schudde, M. Lutz, A. L. Spek, R. Hage, B. L. Feringa, E. Münck and L. Que Jr., *Inorg. Chem.*, 2003, **42**, 2639–2653.

69 M. Martinho and E. Munck, in *Physical Inorganic Chemistry: Principles, Methods, and Models*, John Wiley & Sons, Inc., 2010, pp. 39–67.

70 A. J. Jasniewski and L. Que, *Chem. Rev.*, 2018, **118**, 2554–2592.

71 N. Kitajima, N. Tamura, H. Amagai, H. Fukui, Y. Moro-oka, Y. Mizutani, T. Kitagawa, R. Mathur, K. Heerwegh, C. A. Reed, C. R. Randall, L. Que and K. Tatsumi, *J. Am. Chem. Soc.*, 1994, **116**, 9071–9085.

72 D. M. Kurtz Jr., *Chem. Rev.*, 1990, **90**, 585–606.

73 P. N. Turowski, W. H. Armstrong, S. Liu, S. N. Brown and S. J. Lippard, *Inorg. Chem.*, 1994, **33**, 636–645.

74 I. M. Wasser, C. F. Martens, C. N. Verani, E. Rentschler, H.-W. Huang, P. Moenne-Loccoz, L. N. Zakharov, A. L. Rheingold and K. D. Karlin, *Inorg. Chem.*, 2004, **43**, 651–662.

75 A. Zhou, P. M. Crossland, A. Draksharapu, A. J. Jasniewski, S. T. Kleespies and L. Que Jr., *J. Biol. Inorg. Chem.*, 2018, **23**, 155–165.

76 J. Sanders-Loehr, W. D. Wheeler, A. K. Shiemke, B. A. Averill and T. M. Loehr, *J. Am. Chem. Soc.*, 1989, **111**, 8084–8093.

77 M. D. Clay, F. E. Jenney Jr., H. J. Noh, P. L. Hagedoorn, M. W. W. Adams and M. K. Johnson, *Biochemistry*, 2002, **41**, 9833–9841.

78 H. Park, M. M. Bittner, J. S. Baus, S. V. Lindeman and A. T. Fiedler, *Inorg. Chem.*, 2012, **51**, 10279–10289.

79 C. A. Grapperhaus, M. Li, A. K. Patra, S. Poturovic, P. M. Kozlowski, M. Z. Zgierski and M. S. Mashuta, *Inorg. Chem.*, 2003, **42**, 4382–4388.